


The 26 December 2001 Solar Eruptive Event Responsible for GLE63. II. Multi-Loop Structure of Microwave Sources in a Major Long-Duration Flare

V. Grechnev¹  · A.M. Uralov¹ · V.I. Kiselev¹ ·
A.A. Kochanov¹

Received: 28 June 2016 / Accepted: 24 November 2016
© Springer Science+Business Media Dordrecht 2016

Abstract Our analysis of the observations of the SOL2001-12-26 event, which was related to ground-level enhancement of cosmic-ray intensity GLE63, including microwave spectra and images from the *Nobeyama Radioheliograph* at 17 and 34 GHz, from the *Siberian Solar Radio Telescope* at 5.7 GHz, and from the *Transition Region and Coronal Explorer* in 1600 Å, has led to the following results: A flare ribbon overlapped with the sunspot umbra, which is typical of large particle events. Atypical were i) the long duration of the flare, which lasted more than one hour; ii) the moderate intensity of the microwave burst, which was about 10^4 sfu; iii) the low peak frequency of the gyrosynchrotron spectrum, which was about 6 GHz; and its insensitivity to the flux increase by more than one order of magnitude. This was accompanied by a nearly constant ratio of the flux emitted by the volume in the high-frequency part of the spectrum to its elevated low-frequency part determined by the area of the source. With the self-similarity of the spectrum, a similarity was observed between the moving microwave sources and the brightest parts of the flare ribbons in 1600 Å images. We compared the 17 GHz and 1600 Å images and confirm that the microwave sources were associated with multiple flare loops, whose footpoints appeared in the ultraviolet as intermittent bright kernels. To understand the properties of the event, we simulated its microwave emission using a system of several homogeneous gyrosynchrotron sources above the ribbons. The scatter between the spectra and the sizes of the individual sources is determined by the inhomogeneity of the magnetic field within the ribbons. The microwave

Electronic supplementary material The online version of this article (doi:[10.1007/s11207-016-1025-8](https://doi.org/10.1007/s11207-016-1025-8)) contains supplementary material, which is available to authorized users.

✉ V. Grechnev
grechnev@iszf.irk.ru

A.M. Uralov
uralov@iszf.irk.ru

V.I. Kiselev
valentin_kiselev@iszf.irk.ru

A.A. Kochanov
kochanov@iszf.irk.ru

¹ Institute of Solar-Terrestrial Physics SB RAS, Lermontov St. 126A, Irkutsk 664033, Russia

flux is mainly governed by the magnetic flux passing through the ribbons and the sources. The apparent simplicity of the microwave structures is caused by a poorer spatial resolution and dynamic range of the microwave imaging. The results indicate that microwave manifestations of accelerated electrons correspond to the structures observed in thermal emissions, as well-known models predict.

Keywords Flares · Radio bursts, microwave (mm, cm)

1. Introduction

We continue a study (Grechnev and Kochanov, 2016: Article I) on the 26 December 2001 event (SOL2001-12-26). This solar eruptive-flare event produced a strong flux of solar energetic particles (SEPs, mainly protons) near Earth and the 63rd ground-level enhancement of cosmic-ray intensity (GLE63). GLEs represent the highest-energy extremity of SEPs (see, *e.g.*, Cliver, 2006; Nitta *et al.*, 2012; and references therein). GLEs are rare events; only 72 GLEs have been recorded since 1942. The rare occurrence of GLEs hampers understanding their origins and finding consistent patterns that might govern their appearance and properties.

Unlike electrons, whose signatures are manifold throughout the whole electromagnetic range, accelerated protons and heavier ions can only be detected on the Sun from nuclear γ -ray emission lines appearing in their interactions with dense material (see, *e.g.*, Vilmer, MacKinnon, and Hurford, 2011). Solar γ -ray observations have been very limited in the past. No γ -ray images were available before 2002. Because of the observational limitations, considerations of the origins of SEPs and, especially, GLEs mainly refer to the hypotheses proposed several years ago (see, *e.g.*, Kallenrode, 2003; Aschwanden, 2012 for a review). On the other hand, studies based on recent observations (Cheng *et al.*, 2011; Zimovets *et al.*, 2012; Grechnev *et al.*, 2013a, 2014, 2015b, 2016) indicate that some of these hypotheses might need refinement.

GLEs are typically produced by major eruptive events associated with large flares (mostly of GOES X-class), fast coronal mass ejections (CMEs), and strong microwave bursts. The common association with different solar energetic phenomena (Kahler, 1982; Dierckx *et al.*, 2015; Trotter *et al.*, 2015) hampers the identification of the origins of SEPs and GLEs. All of these circumstances show how important the analysis of a solar source of each GLE is.

With a general correspondence between the magnitudes of SEPs, CME speeds, and flare manifestations, there are few outliers from the correlations (Grechnev *et al.*, 2013a, 2015a). Strong fluxes of high-energy protons were observed near Earth after these events associated with moderate microwave bursts. The correlation between the proton fluences, on the one hand, and microwave and soft X-ray (SXR) fluences, on the other hand, is considerably higher. This is difficult to understand if SEPs are exclusively shock-accelerated. A flare-related contribution could also be significant in the events, whose proton productivity was enhanced for some unclear reasons. One of these events was the SOL2001-12-26 eruptive-flare event that was responsible for GLE63.

This solar event has not been comprehensively studied because only limited observations are available. We are not aware of either low-coronal observations of an eruption or hard X-ray (HXR) data. On the other hand, the event was observed in microwaves by the *Siberian Solar Radio Telescope* (SSRT: Smolkov *et al.*, 1986; Grechnev *et al.*, 2003) at 5.7 GHz, by the *Nobeyama Radioheliograph* (NoRH: Nakajima *et al.*, 1994) at 17 and 34 GHz, and in the ultraviolet (UV) by the *Transition Region and Coronal Explorer* (TRACE: Handy *et al.*, 1999).

The SSRT observations have been studied in [Article I](#). The conclusions of this article are as follows:

- i) Most likely, GLE63 was caused by the M7.1 solar event in active region (AR) 9742 (N08 W54). Contribution from a concurrent far-side event is unlikely.
- ii) The flare was much longer than other GLE-related flares and consisted of two parts. The first, possibly eruptive, flare and a moderate microwave burst started at 04:30 and reached an M1.6 level. The main flare, up to M7.1, with a much stronger burst, started at 05:04, when a CME was launched.
- iii) The main flare involved strong magnetic fields presumably associated with a sunspot in the western part of AR 9742.
- iv) Two nonthermal sources observed at 5.7 GHz initially approached each other nearly along the magnetic neutral line, and then moved away from it like expanding ribbons, as if they were associated with the legs of the flare arcade.

It was difficult to confirm and expand these indications in [Article I](#) based solely on the SSRT data because of their insufficient spatial resolution and coalignment accuracy. To verify and elaborate these results, observations of the flare arcade or ribbons in a different spectral range, where they are clearly visible, need to be compared with microwave data of a higher spatial resolution.

Of special interest is a conjectured localization of the nonthermal microwave sources in the legs of the flare arcade. This possibility does not contradict the commonly accepted view on the flare process; however, HXR and microwaves almost always show a few simple nonthermal sources. Ribbon-like HXR structures have been observed in exceptional events (Masuda, Kosugi, and Hudson, 2001; Liu *et al.*, 2007). The simplicity and confinement of nonthermal sources in impulsive flares suggested involvement of one to two loops (Hanaoka, 1996, 1997; Nishio *et al.*, 1997; Grechnev and Nakajima, 2002). Later observational studies extended this view up to some long-duration flares (Tzatzakis, Nindos, and Alissandrakis, 2008). A concept of a single microwave-emitting loop became dominant.

One of the main purposes of our companion articles is to determine the possible causes of the contrast between the rich proton outcome of this solar event and its moderate manifestations in microwaves. We consider *a priori* the contributions from the acceleration processes both in the flare and by the shock wave to be possible (Grechnev *et al.*, 2015a). Accordingly, we examine the 26 December 2001 flare in this article (Article II) and the eruptive event in Article III (Grechnev *et al.*, 2017). Here we endeavor to shed further light on the listed issues related to the flare itself and its microwave emission by analyzing the observations carried out by TRACE at 1600 Å and by NoRH at 17 and 34 GHz.

2. Observations

2.1. Parts of the Flare

TRACE observed the flare mostly in the 1600 Å channel, which we use. The 1600 Å images are similar to those observed in the H α line, but they do not show filaments. Some images were produced less often in other UV channels, 1550 and 1700 Å, and in white light. The whole set that we analyze consists of 668 images observed in 1600 Å from 04:23 to 05:22 (all times hereafter refer to UTC). The imaging interval between 63 images from 04:23 to 04:55 was around 30 seconds, and then it decreased to about 2 seconds from 05:04 to 05:22. The exposure time was 0.43 seconds before 04:30, then 0.26 seconds until 05:00, and it changed cyclically between 0.020, 0.031, and 0.052 seconds during the main flare.

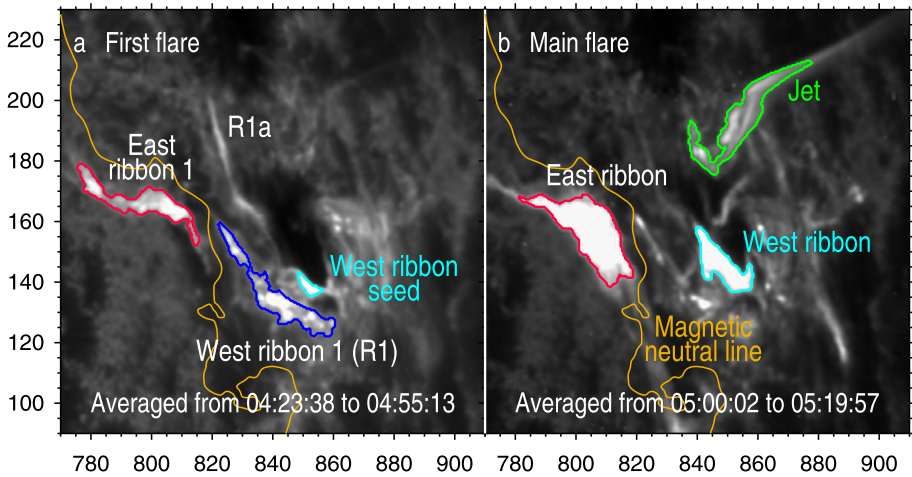


Figure 1 Averaged TRACE 1600 Å images showing the regions involved in the first flare (a) and main flare (b). The orange contour traces the magnetic neutral line at the photospheric level. a) The ribbons in the first flare (red and blue contours). The light-blue contour outlines a seed of the west ribbon, which evolved in the main flare. b) The ribbons in the main flare (red and light-blue contours). The green contour outlines a jet and a part of its base. The axes show the coordinates in arcsec from the solar disk center.

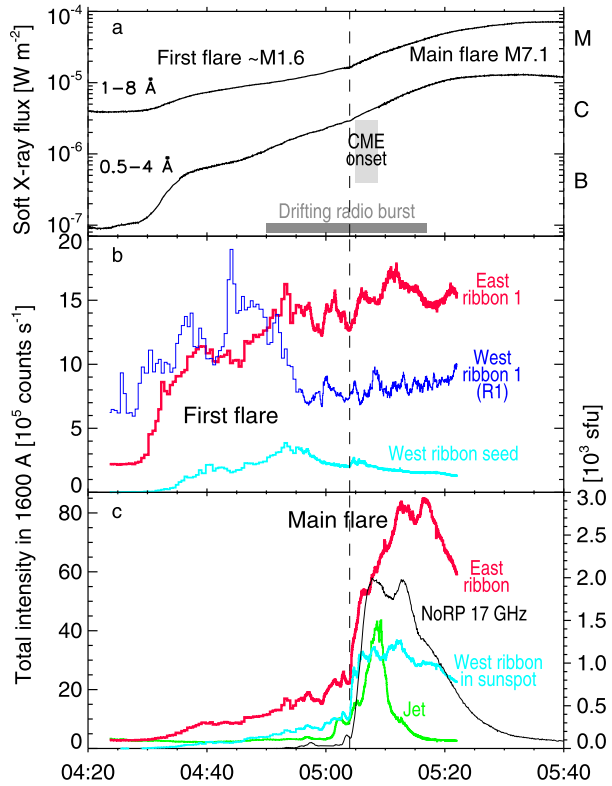
A [2001-12-26_TRACE_1600A.mpg](#) movie in the electronic supplementary material presents the whole flare observed in 1600 Å.

We processed the TRACE images as follows: The background level was found for each image as a highest-probability value in its histogram. This individual level was subtracted from each image, which was converted into a reference exposure time of 0.43 seconds. The offset between the 1600 Å and white-light channels was corrected for their coalignment. A comparison with white-light images produced by the *Michelson Doppler Imager* (MDI; Scherrer *et al.*, 1995) onboard SOHO revealed a roll angle of 0.9° in the TRACE images, which was compensated for, and refined their absolute pointing coordinates. All of the images were transformed to 05:04 to compensate for the solar rotation. Bright defects produced by high-energy particles were reduced in calculations by using a minimum of two images separated by a small interval (Grechnev, 2004). Any remaining issues of the processing described here are insignificant.

The main flare configurations are presented by the TRACE images averaged during each of the two flare parts in Figures 1a and 1b. The images are shown within a limited brightness range and scaled by a power-law function with a γ of 0.7. The dark region near the centers of the panels corresponds to a sunspot. The orange contour traces the main magnetic-polarity inversion (neutral) line at the photospheric level calculated from a SOHO/MDI magnetogram observed on 26 December at 04:51.

The averaged images and movie present complex flare configurations. The first flare started from the appearance of two extended thin ribbons at both sides of the neutral line (a remote northeast brightening is beyond the field of view of Figure 1). The east ribbon evolved in the first flare within the red contour. Three structures are magnetically conjugate to the east ribbon. A long thin ribbon R1a was active early in the event, and then it faded smoothly. We do not consider this region. Intermittent brightenings within the dark-blue contour were active during the first flare, and then became less important. A small bright region started to grow near the sunspot (light-blue contour).

Figure 2 Flare light curves recorded by GOES in soft X-rays (a) and those computed from the TRACE 1600 Å images over the flaring regions in the first flare (b) and main flare (c). The colors of the curves correspond to those of the regions in Figure 1. Two distinct flare parts are separated by the dashed line. The gray bars in panel a represent the observation interval of a slowly drifting radio burst and the CME onset time extrapolated to the position of AR 9742. The black curve in panel c represents the background-subtracted total flux at 17 GHz.



In the main flare, the east ribbon broadened and extended southwest (Figure 1b). The west-ribbon seed broadened northwest and became the main west ribbon. A jet (green contour) appeared after 05:06 in a funnel-like configuration with a ring base, along which brightenings ran in the movie. Such funnels appearing above magnetic islands inside opposite-polarity regions contain coronal null points (Masson *et al.*, 2009; Meshalkina *et al.*, 2009). The magnetic structure of a small flux-rope erupting inside a funnel cannot survive at a null point (Uralov *et al.*, 2014), and released plasma flows out as a jet (Filippov, Golub, and Koutchmy, 2009). The collision of an erupting flux-rope with a separatrix surface can produce a shock wave (Meshalkina *et al.*, 2009; Grechnev *et al.*, 2011).

Figure 2 shows the flare light curves and milestones of the event. An inflection in the GOES channels in Figure 2a separates the two parts of the flare. The separation time is close to the CME onset time of 05:06–05:10 extrapolated to 1 R_⊙ in the CME catalog (cdaw.gsfc.nasa.gov/CME_list/; Yashiro *et al.*, 2004) based on the data from the SOHO's *Large Angle and Spectroscopic Coronagraph* (LASCO; Brueckner *et al.*, 1995). The heliocentric distance of the flare site was 0.864 R_⊙. With an average CME speed of 1446 km s⁻¹, its onset time at the flare site should be 65 seconds earlier (the light-gray bar in Figure 2a). The association of the CME with the main flare was previously found by Gopalswamy *et al.* (2012).

A slowly drifting Type II and/or Type IV burst was associated with the event. In the Learmonth spectrum up to 180 MHz shown by Nitta *et al.* (2012), the burst is detectable from about 04:57, too early for the fast CME. The burst can be followed back until 04:50 up to 300 MHz in the *Hiraiso Radio Spectrograph* (HiRAS) spectrum (2001122605.gif) at

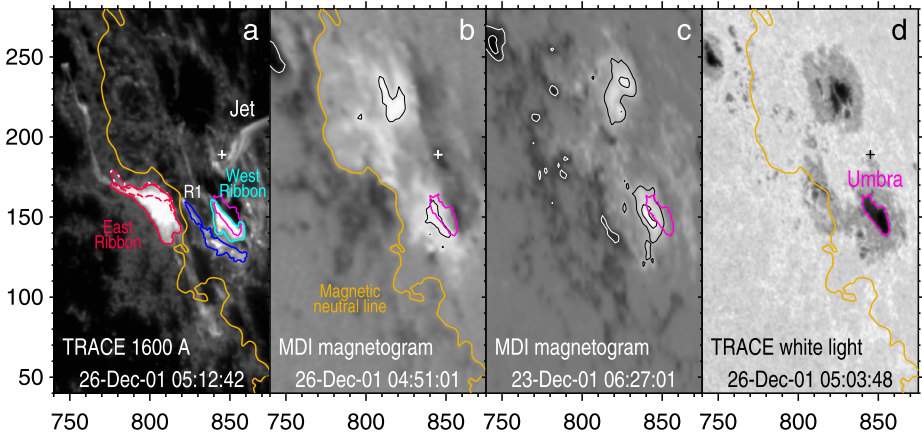


Figure 3 Comparison of the flare configuration visible in a TRACE 1600 Å image (a) with the MDI magnetograms observed on 26 December (b) and 23 December (c) as well as a TRACE white-light image (d), all transformed to their appearance at the onset time of the main flare of 05:04. The broken red–white contour and the dark-blue contour outline the ribbons observed in the first flare. The orange contour traces the magnetic neutral line. The pink contour outlines the sunspot umbra. The contour levels for the magnetograms are [$\pm 1000, \pm 2000$] G (black N-polarity, white S-polarity). The crosses in panels a, b, and d mark the base of the jet. The axes indicate the distance from solar disk center in arcseconds.

sunbase.nict.go.jp/solar/denpa/hirasDB/Events/2001/ (the dark-gray bar in Figure 2a). This burst could only be caused by expanding ejecta or a wave, which started well before the fast CME from AR 9742. No other CME was detected around that time. Most likely, this burst was caused by a slower eruption that preceded the fast CME.

Figures 2b and 2c present the light curves for the first and main flare, respectively, calculated from the TRACE 1600 Å images as the total over the main flare regions denoted in Figures 1a and 1b. The bars represent the imaging intervals. The black curve in Figure 2c shows a microwave burst recorded by the *Nobeyama Radio Polarimeters* (NoRP; Torii *et al.*, 1979; Nakajima *et al.*, 1985) at 17 GHz.

The flare has two distinct parts. The first flare started at about 04:30 and lasted ≈ 34 minutes before the main flare. The 17 GHz burst did not exceed 200 sfu. The main flare started at about 05:04 with a sharp increase in the UV emissions from the two main ribbons and the 17 GHz burst. The temporal profiles of the west ribbon and the microwave burst are similar, but not identical.

2.2. Photospheric Configuration

Figure 3 compares the configuration observed in 1600 Å near the flare peak with MDI magnetograms and a white-light TRACE image produced at the main flare onset. The field of view presents the total length of the east ribbon with its remote extensions into a northeast S-polarity sunspot and a southwest region of weak magnetic fields. The color contours correspond to Figure 1. The red–white dashed contour denotes the east ribbon in the first flare. The pink contour corresponds to the N-sunspot umbra in Figure 3d. In the main flare, the west ribbon overlapped the sunspot umbra in Figure 3a, as Article I assumed.

The magnetogram of AR 9742 located not far from the limb is affected by projection effects on the magnetic field inclined toward the line of sight. To find realistic fields, we consider the magnetograms that were observed immediately before the main flare (Figure 3b)

and three days before (Figure 3c). The magnetograms are scaled by a power-law function with a γ of 0.8 for each polarity separately (bright = positive, dark = negative).

AR 9742 evolved over three days. The main magnetic-field distribution persisted. The changes are mostly related to weaker-field regions and the shape of the neutral line. The S-polarity field under the future east ribbon concentrated. The flare-related south N-sunspot became slightly displaced.

The magnetograms exhibit three types of distortions: i) Unlike the magnetogram in Figure 3c, the west parts of the sunspots in Figure 3b appear with a spurious inverted polarity (this is a common feature in magnetograms close to the limb). ii) The field strengths in Figure 3b are reduced vs. Figure 3c in both sunspots and plage regions, and a secant correction seems to be justified for all of the regions. iii) A hook-like shape of the 2000 G contour in the south sunspot indicates a saturation-like distortion occurring in MDI magnetograms. This distortion is also present in the 26 December magnetogram. With a maximum field strength of 2807 G observed there on 23 December, the real strength in the south sunspot could reach ≈ 3000 G vs. 1164 G in the 26 December magnetogram.

The cross in Figure 3a denotes the base center of the funnel-like configuration where the jet occurred. Figure 3b shows an island of an enhanced magnetic field of up to -855 G at this location. The magnetograms of the preceding days indicate that this was most likely a negative-polarity island inside a positive environment.

2.3. Microwave Observations

The microwave burst was observed at a number of fixed frequencies by the NoRP and Learmonth radiometers. These data allow us to analyze the spectrum of the burst. We did not use the NoRP data at 80 GHz, which look unreliable. To cross-calibrate the NoRP and Learmonth data, the background-subtracted flux at each frequency was integrated from 04:20 to 05:30. The logarithmic spectrum was fitted with a fifth-order polynomial, and the deviations from the fit were used as cross-calibration coefficients, which ranged between 0.87 and 1.21.

Figures 4a–4d present total-flux temporal profiles at four frequencies. The gyrosynchrotron (GS) temporal profile extends to a very low frequency of 610 MHz. A spiky component is due to plasma emission, and late-phase enhancements at 610 MHz and 2 GHz are probably due to a Type IV burst from a different source.

The spectra in Figure 4e were calculated with an integration time of 50 seconds for the four times denoted in the upper panels. The spectra are similar, although the ratio of the peak fluxes between the solid and the dotted curve reached 18. The peak frequency estimated from a sixth-order polynomial fit was $6.1 \text{ GHz} \pm 5 \%$. The low-frequency branch was elevated relative to the slope of 2.9 for a classical GS spectrum (gray curve) and had an actual slope of ≤ 1.8 at frequencies ≥ 1.4 GHz. The elevation could be due to inhomogeneity of the emitting source, *i.e.* increasing at lower frequencies through the contribution from higher layers, where the magnetic field is weaker (see, *e.g.*, Lee, Gary, and Zirin, 1994; Kundu *et al.*, 2009 and references therein). The high-frequency slope $[\alpha]$ corresponds to a power-law index $\delta = (1.22 - \alpha)/0.9 \approx 3$ of the electron-number spectrum, according to Dulk and Marsh (1982).

Figures 5a and 5b show the total flux and maximum brightness temperatures of microwave sources measured at 17 and 34 GHz from NoRH images and at 5.7 GHz from SSRT images (see Article I). Figure 5c presents the total area of the sources at 17 and 34 GHz. The only way to increase the flux of a simple GS source while keeping its spectrum shape is to increase its area (Dulk and Marsh, 1982; Stähli, Gary, and Hurford, 1989) with an unchanged brightness temperature. Figure 5 presents an opposite relation. When the total flux

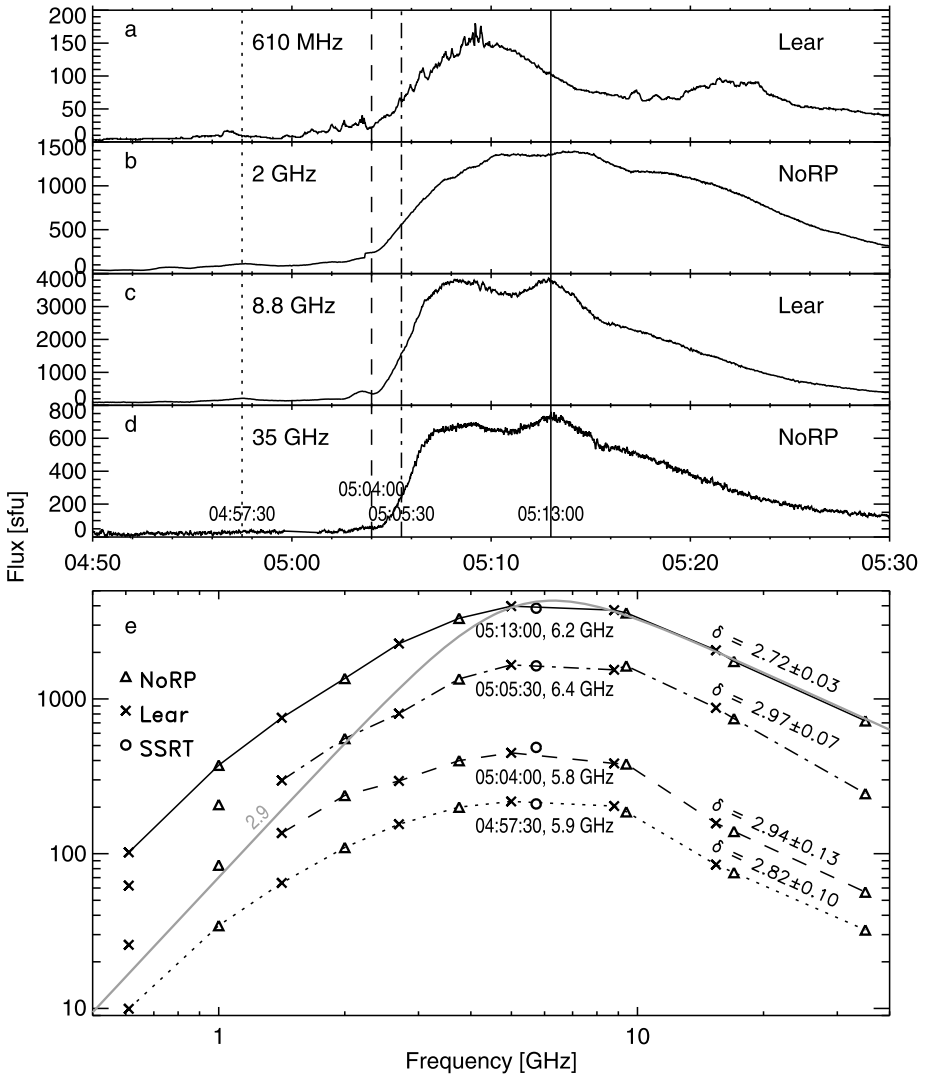


Figure 4 a–d) Total-flux temporal profiles of the burst at four radio frequencies. e) The spectra for the four times denoted in panels a–d by the lines of the corresponding styles. The observation time, estimated peak frequency [ν_{peak}], and a power-law index of microwave-emitting electrons [δ] are specified for each spectrum. The gray curve represents a classical GS spectrum corresponding to the high-frequency observations at the peak of the burst.

and brightness temperature strongly increased between times b and c, the change in the total area of the sources was minor. Figure 5c also indicates that each of the microwave sources might not be well resolved. This complicates the situation.

2.4. Motions of Microwave Sources and UV Ribbons

To obtain indications of microwave-emitting structures, we consider bright kernels in 1600 Å as footpoints of the loops, with whose legs microwave sources could be associated.

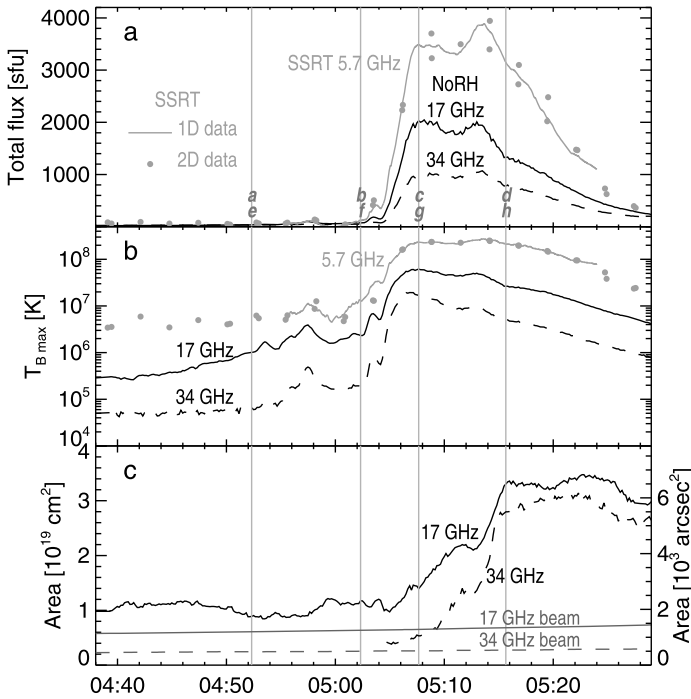


Figure 5 Temporal profiles of microwave sources observed at 17 GHz (solid), 34 GHz (dashed), and at 5.7 GHz (gray): a) total flux, b) maximum brightness temperature, c) total area (NoRH only). The nearly horizontal lines in panel c represent the areas of the half-height NoRH beam at 17 and 34 GHz. The labels at the bottom of panel a denote the imaging times in Figure 6.

Figures 6a–6d show the 1600 Å images overlaid by contours of the 17 GHz images (see also the [2001-12-26_NoRH_TRACE_kernels.mpg](#) movie with contours at $[0.1, 0.3, 0.9]T_{Bmax}$ over each 17 GHz image). Figures 6e–6h reveal bright kernels in 1600 Å that are emphasized by subtracting the images observed two minutes before, along with the outermost 17 GHz contours. With a position of the flare site at N08 W54, the microwave sources in the low corona must be offset west-northwest from the upper-chromosphere 1600 Å images. The offset uncertainty can reach 10'', while the coalignment accuracy is presumably within 5'' in the 17 GHz images and within 1'' in the UV images.

Two microwave sources in Figures 6a–6d reside above two ribbons located in opposite magnetic polarities. Such sources are commonly interpreted as the conjugate legs of a single loop. However, different clusters of bright kernels in Figures 6e–6h correspond to different sets of loops dominating at each of the four times. A comparison of the thick contours and the NoRH beam (both at a half-height level) shows that these sets of loops were unresolved by NoRH. If the two 17 GHz sources were located in the legs of multiple loops, then correspondence would be expected between the relative positions of the ribbons, on the one hand, and those of the microwave sources, on the other hand.

Indications of this correspondence were found in Article I from the relative motions of the two sources observed in SSRT images at 5.7 GHz. Here we elaborate on this result using the measurements from the 1600 Å and 17 GHz images. For the measurements at 17 GHz we used the same technique as in Article I. For each ribbon we used the centroid of its current image in 1600 Å within the 10 % contour of the ribbon averaged over the whole flare.

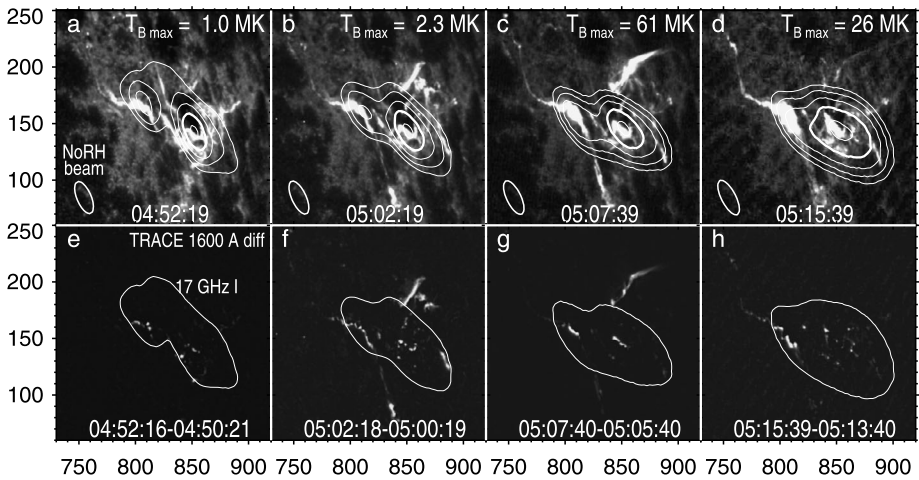


Figure 6 Top: four flare episodes in 1600 Å (background) and 17 GHz images (contours) denoted in Figure 5. Contour levels are at $[0.0625, 0.125, 0.25, 0.5, 0.9]T_{B \max}$ specified in each panel. The thick contour is at a half-height level. The ellipses represent the half-height contours of the NoRH beam. Bottom: two-minute running-difference 1600 Å images and 0.0625-level contours of the 17 GHz images. Solar rotation was compensated for in all images to 05:04. The axes indicate the distance from solar disk center in arcseconds.

Figure 7 a) Temporal variations in distance between the centers of the two sources observed at 17 GHz (NoRH: gray) and 5.7 GHz (SSRT: circles) in comparison with those for the flare ribbons in 1600 Å (TRACE, black). The vertical bars represent the full widths at half maximums (FWHM) of the SSRT and NoRH beams in the east–west direction. b) The angle between the line connecting the centers of the two sources and the main orientation of the magnetic neutral line (105°). The accuracy of the results denoted by the open circles can be reduced by overlap between the images of the sources produced by the SSRT.

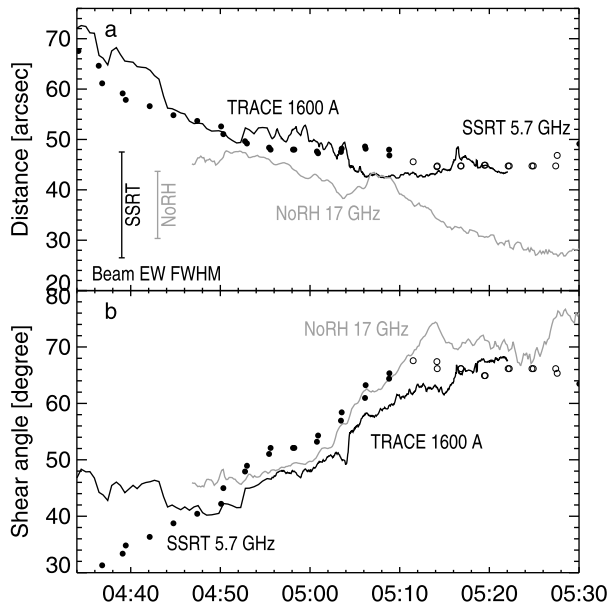


Figure 7 shows the distance between the microwave sources and their position angle relative to the main orientation of the neutral line (105° from the West) measured from the 5.7 and 17 GHz images and the same parameters of the ribbons in 1600 Å. These relative measurements do not depend on any coalignment accuracy. The east 17 GHz source was absent before 04:46:50, and our analysis of the TRACE data ends at 05:22:04. The vertical bars in Figure 7a show that the variations of the distances are well below the beam size of

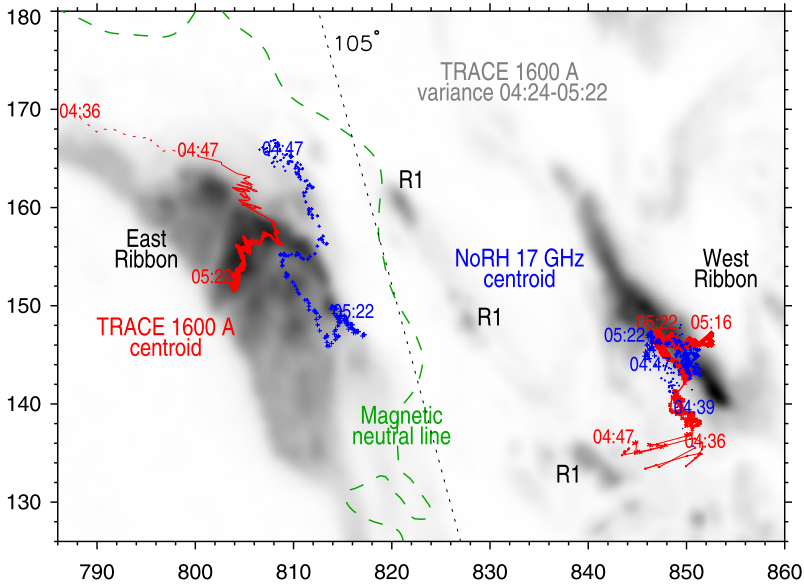


Figure 8 Motions of of the flare ribbons (centroids) in 1600 Å images (red) and those of the 17 GHz sources (blue). The gray-scale background presents a negative variance image computed over both flare parts. Faintly visible parts of the west ribbon in the first flare are denoted R1. The temporal succession is indicated by the increasing thickness of the line (1600 Å) and size of the symbols (17 GHz). The green-dashed line represents the magnetic neutral line. The dotted line inclined by 105° to the West is a reference direction in the measurements of the shear angle in Figure 7b. See also the [2001-12-26_NoRH_TRACE_kernels.mpg](#) movie. The axes indicate the distance from solar disk center in arcseconds.

both SSRT and NoRH. This fact does not contradict the instrumental resolution, because we measure the centroid of a source rather than its structure, but it makes the results sensitive to imaging issues and changes in the shapes of the sources.

The main tendencies observed in the three spectral ranges are similar from 04:45 until 05:15. The microwave spectra in Figure 4e are also similar in this interval. The decrease in distance between the 17 GHz sources in Figure 7a after 05:10, dissimilar to the others, is probably due to an increasing emission from all the low loops that are filled with trapped higher-energy electrons. This is less pronounced in the lower-frequency SSRT images and absent in the 1600 Å images. It is difficult to separate this contribution from the main sources at 17 GHz. The measurements from the SSRT data denoted by the open circles are complicated by overlap of the sources (Article 1). The difference between the measurements from the 5.7 GHz and UV data in Figure 7b before 04:45 is due to two causes. The first, geometrical, cause is the location of the UV ribbon centroid near a bend of the neutral line (Figures 1 and 3) that distorts the measured shear angle. Second, the magnetic field in this region was insufficient to produce a detectable gyromagnetic emission, and the 5.7 GHz centroid was displaced to stronger magnetic fields. With the complications that we mentioned, the relative motions of the microwave sources and flare ribbons were similar.

This correspondence allows us to compare the measured centers of the 17 GHz sources and UV ribbons. We do not use the positions of the microwave sources here that were measured from SSRT images because their pointing accuracy is insufficient. Figure 8 presents the trajectories of the microwave sources (blue) and UV ribbons (red). Their increasing thickness or size indicates time, which is also specified at some positions. The gray-scale

background is a negative variance image computed from all TRACE images obtained during the whole flare. This image represents all changes observed in 1600 Å according to their statistical contributions (Grechnev, 2003). The green-dashed line represents the neutral line.

The variance image clearly shows the main east ribbon, which extended south and broadened east, and the main west ribbon in the main flare. The initial west ribbon in the first flare (R1) appears in Figure 8 as three fragments.

The red-dotted line represents the centroid of the east ribbon before 04:47, when its microwave counterpart was absent. The east-ribbon centroid moved nearly parallel to the neutral line from 04:36 to a hump, and then turned away from the neutral line. The trajectory of the east microwave source is mostly parallel to that of the east ribbon centroid. A later divergence is due to increasing contribution to microwaves from the upper part of the arcade. The offset of the microwave sources from the UV ribbons is due to their different heights.

The west part of the flare site was more complex. Intermittent brightenings on ribbon R1 during the first flare flipped the centroid between R1 and west-ribbon seed. The west microwave source was more stable because of a strong direct dependence on the magnetic field. In the main flare, both the west ribbon and microwave source drifted to the strongest-field region above the sunspot umbra. An excursion of the ribbon centroid around 05:16 was due to a brightening at the southwest edge of the sunspot that we did not consider.

The agreement between the trajectories observed in 1600 Å and at 17 GHz cannot be a coalignment issue because the west microwave source was localized from 04:47 to 05:22 within 6", while the east microwave source was systematically displaced during this interval by 14" (excluding the later mismatching part of its trajectory). The trajectories of the ribbons and microwave sources correspond to each other, except for the mentioned deviations, whose causes are clear.

The measurements of the shear angle between the UV ribbons were initially affected by an eastward bending of the neutral line. When we imagine that this part of the neutral line is straightened and the easternmost part of the east ribbon maintains the direction of 105° everywhere, then the initial angle would decrease substantially. Thus, the overall decrease in shear throughout the event exceeded the 40° we measured.

2.5. Comparison of Microwave and UV Images

The correspondence between the UV ribbons at the bases of the arcade and microwave sources above the ribbons confirms the association of the microwave sources with the legs of the arcade loops. Nonthermal electrons precipitating in dense layers are ultimately responsible for the UV emission. On the other hand, both precipitating and trapped nonthermal electrons radiate GS emission in the low-corona magnetic loops. The UV and microwave emissions depend in opposite senses on the magnetic-field strength [B]. With an estimated electron spectrum index of $\delta \approx 3$, the GS emissivity at optically thin frequencies has a direct dependence $\propto B^{2.5}$ (Dulk and Marsh, 1982), whereas the well-known mirroring in strong magnetic fields hampers electron precipitation, which governs the UV emission.

The real physical distinction between the structures emitting in these two spectral ranges and responsible processes might be emphasized by different instrumental characteristics of TRACE and NoRH. To verify this idea, the difference in the spatial resolution can be compensated for by convolving the TRACE images (1" resolution) with a NoRH beam. Its cross section is an ellipse whose parameters gradually change during the observing day. At 05:02 on 26 December, its half-height dimensions were 12.7" \times 31.4" (we used the NoRH images synthesized at 17 GHz by the enhanced-resolution Fujiki software).

Figure 9 shows the results of our experiment for four different flare episodes. The left column presents the TRACE 1600 Å images, the right column presents nearly simultaneous

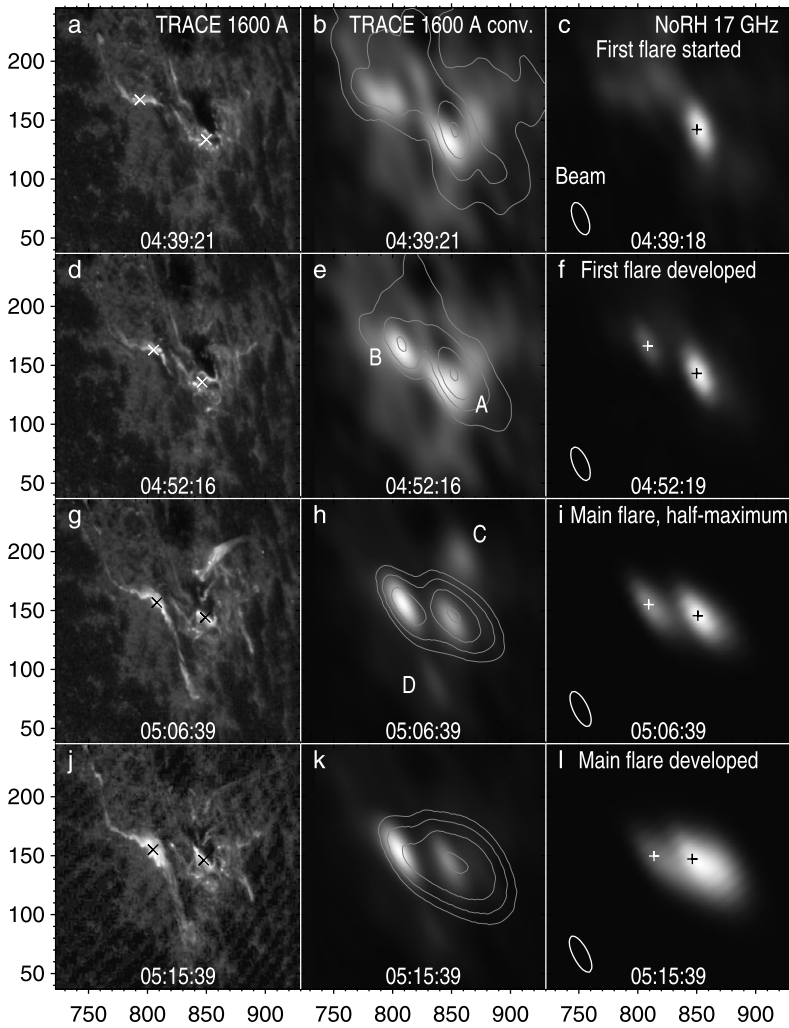


Figure 9 Comparison of TRACE 1600 Å images (left column, logarithmic brightness scale) with NoRH 17 GHz images (right column, linear scale). The middle column (linear scale) shows the 1600 Å images convolved with the NoRH beam (ellipses in the right panels) overlaid with contours of the microwave images. Contour levels in each image are at 0.9 of its maximum divided by powers of 3. The centroid of each ribbon is denoted in the left column by the slanted cross. The centroid of each microwave source is denoted in the right column by the straight cross. The axes indicate the distance from solar disk center in arcseconds.

NoRH images, and the middle column presents the TRACE images convolved with the NoRH beam, whose elliptic half-height contours are shown in the right panels. To facilitate comparison, the convolved images in the middle column are overlaid with contours of the microwave images.

The structures in Figures 9b and 9c are similar. A subtle counterpart of the east ribbon is also detectable at 17 GHz. The environment in weaker fields is faint but detectable in microwaves, as the contours in Figure 9b indicate.

The main sources in Figures 9e and 9f are also similar. A brighter microwave source [A] is located in the stronger magnetic field. Conversely, the image of the weaker-field east ribbon [B] is brighter in the convolved UV image, as expected.

The presence of additional features C and D in Figure 9h makes it dissimilar to Figure 9i. Feature C is the jet emanating from a configuration with a magnetic null point. The magnetic-field strength there steeply falls off upward, and a microwave counterpart is not expected. Feature D is the southernmost end of the east ribbon located in a weak magnetic field. Its absence in microwaves is not surprising, especially with a limited dynamic range of NoRH of about 300.

The images in Figures 9k and 9l become less similar because the upper part of the coronal arcade appears at 17 GHz, but is invisible in the UV. The brightness temperature of the arcade in Figure 9l exceeded the 15 MK estimated for this time from GOES data in Article I; the power-law index of its brightness temperature spectrum estimated from the images at 17 and 34 GHz was around -2.7 . Therefore, thermal bremsstrahlung could only supply a minor contribution. Most likely, the upper part of the arcade was dominated by trapped electrons with a harder spectrum, consistent with a general pattern established by Kosugi, Dennis, and Kai (1988), Melnikov and Magun (1998), and in later studies.

In summary, the microwave sources A and B were most likely associated with the legs of the arcade rooted in the ribbons. Bright kernels in 1600 \AA represented instantaneous loci of the electron precipitation. Electrons trapped in numerous loops, whose footpoints were shown by the UV kernels previously, emitted a prolonged background GS emission. This long-lasting background reinforced the similarity between the images of the long-lived flare ribbons and the microwave sources.

2.6. Microwave Spectral Evolution

This possible scenario should be manifested in the evolution of the microwave spectrum. In addition to the detailed GS spectra presented in Figure 4e for four times, here we examine the overall variations of the peak frequency [ν_{peak}] and a power-law index of microwave-emitting electrons [δ] for the whole flare.

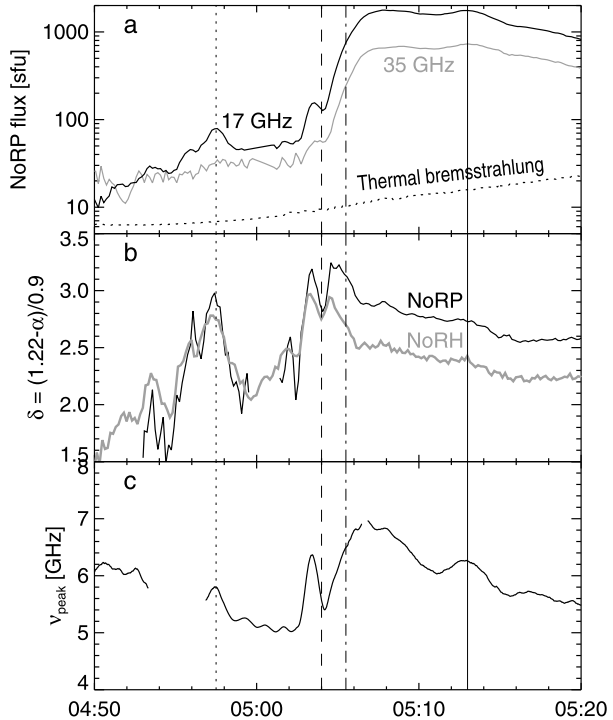
The δ -index of the electron-number spectrum can be calculated as $\delta = (1.22 - \alpha)/0.9$ (Dulk and Marsh, 1982); α should be estimated from optically thin data, *e.g.* from the total flux NoRP data at 17 and 35 GHz or from NoRH images at 17 and 34 GHz. We used both methods because the NoRP data are characterized by a higher accuracy, while the NoRH data provide a higher sensitivity. The contribution of thermal bremsstrahlung was subtracted. The result was smoothed over ten seconds.

The peak frequency was estimated in a way similar to the technique used by White *et al.* (2003) and Grechnev *et al.* (2008, 2013a) from NoRP and Learmonth total-flux data (Section 2.3). For each time, a combined spectrum at 12 frequencies was averaged over 16 seconds, and a parabola was fitted to the five points of the log-log spectrum closest to the peak. The result was smoothed over 30 seconds.

Figure 10 shows the 17 and 35 GHz fluxes along with an estimated thermal flux, and the calculated ν_{peak} and δ . The intervals with doubtful estimates were rejected. The values of δ estimated from NoRH data are more reliable than those from NoRP data for weaker fluxes, and conversely for stronger fluxes.

The electron index [δ] in Figure 10b has an impulsive component superposed on a harder gradual background. The initial values of $\delta \approx 1.5-2.0$ are too hard, probably because the thermal flux from the GOES data is underestimated. They are insensitive to plasma temperatures of $\lesssim 3 \text{ MK}$, whose contribution to microwaves can be considerable. Its possible role is

Figure 10 Evolution of the microwave emission during the event. a) Total-flux temporal profiles recorded by NoRP at 17 and 35 GHz. The dotted line represents thermal bremsstrahlung estimated from GOES data. b) Power-law index of microwave-emitting electrons computed from NoRP (black) and NoRH (gray) data. c) Variations in microwave peak frequency. The vertical lines mark the four times presented in Figure 4 with corresponding styles.



expected to decrease as the GS emission increased. The GS emission from trapped electrons with a progressively hardened spectrum in the course of a continuous injection probably dominated late in the event. The trapping effect could also affect the initial part of Figure 10b because the flare lasted for about 20 minutes before 04:50. The comparison of Figures 10a and 10b shows that the impulsive component corresponds to enhancements in the time profiles. Most likely, freshly injected electrons had a softer spectrum with $\delta \approx 3.5-4.0$, which did not change considerably throughout the flare. The probable power-law index of microwave-emitting electrons was typically $\delta \approx 2.5-3.3$.

The peak frequency in Figure 10c varies in a range of 5–7 GHz. The values of ν_{peak} (and δ in Figure 10b) at the four marked times are close to those estimated in Figure 4e in a slightly different way. The evolution of ν_{peak} suggests an interplay of the parameters of emitting electrons and magnetic-field strength; however, the range of ν_{peak} seems to be atypically narrow and low for the observed microwave fluxes. A possible key to these challenges could be a distributed microwave-emitting system. The average ν_{peak} of individual sources was around 6 GHz, and their total number elevated the peak flux of each one up to the observed values. The scatter between the parameters of the sources could be a reason for the broadening of the microwave spectrum and its gradual shape.

3. Discussion

The analysis of the microwave and UV images has shown that each of the two microwave sources observed at 5.7, 17, and 34 GHz was associated with one of the two ribbons located in opposite-polarity magnetic fields. The appearance of each microwave source corresponds

to the whole related ribbon, as it has been viewed by NoRH. The ribbons and microwave sources both exhibited nearly identical systematic motions. Until the peak of the microwave burst, the two flare centers approached each other nearly along the neutral line, so that the distance and shear between them decreased considerably. After that, the motion occurred away from the neutral line, corresponding to the usual expansion of the ribbons. The expansion was measured from the SSRT data until 06:30 in [Article I](#).

The correspondence of each microwave source to the flare ribbon, their nearly identical motions, and the surprisingly persistent shape of the microwave spectrum in spite of the 18-fold flux variations indicate that microwaves were emitted by the conjugate legs of multiple loops that constituted the flare arcade. The relation of the magnetic-field strengths below the ribbons points to a strongly asymmetrical configuration. Magnetic-flux conservation in flare loops requires larger areas of the sources above the weaker-field east ribbon relative to their conjugate counterparts above the sunspot-associated west ribbon. To verify these considerations, we will attempt to reproduce the observed spectra by means of a simple model, using the magnetic fields that are actually measured.

3.1. Reconnection Power and Flux of GS Emission

The microwave flux density $[F(t)]$ at optically thin frequencies $[\nu > \nu_{\text{peak}}]$ is controlled by the instantaneous total number of emitting high-energy electrons $[N_{\text{tot}}(t)]$. The self-similarity of the spectra in a wide range of microwave fluxes in [Figure 4e](#) shows that the $N_{\text{tot}}(t) \propto F(t)$ relation in this event also applied at lower frequencies $[\nu \leq \nu_{\text{peak}}]$. Accelerated electrons are produced in a reconnection process; therefore, $N_{\text{tot}}(t)$ is associated with a power of flare energy release. We determine below which observable parameters of a flare indicate this association.

The energy flux density entering the flare current sheet from one of its sides is governed by the Poynting vector: $\mathbf{P} = c[\mathbf{E} \times \mathbf{B}]/4\pi = -[[\mathbf{v} \times \mathbf{B}] \times \mathbf{B}]/4\pi = [\mathbf{v}B^2 - \mathbf{B}(\mathbf{B} \cdot \mathbf{v})]/4\pi = \mathbf{v}B^2/4\pi$ [erg cm⁻² s⁻¹]. Here $\mathbf{E} = -[\mathbf{v} \times \mathbf{B}]/c$; \mathbf{B} is a vertical magnetic field, *i.e.* $\mathbf{B} = B_z$; \mathbf{v} is the horizontal velocity of the plasma inflow into the vertical current sheet, *i.e.* $\mathbf{v} = v_x$.

The total power released in the current sheet dimensioned Y by Z is $q = 2PYZ = vB^2YZ/2\pi = BZBY(dx/dt)/2\pi = BZ(d\Psi/dt)/2\pi$ [erg s⁻¹]. Here $d\Psi = BYdx$, and $d\Psi/dt$ is the input rate of the magnetic flux.

Let τ be the lifetime of a point-like UV kernel in the footpoint of a thin magnetic tube during reconnection in the current sheet and afterward. A multitude of kernels constitutes an instantaneous UV-emitting stripe corresponding to a narrow moving flare ribbon in the standard model. Then, $\tau d\Psi/dt = \Psi(\tau, t)$, which is the magnetic flux within the ribbon stripe at time t . Presumably, τ is proportional to the lifetime of accelerated electrons in the magnetic tube, and $\Psi(\tau, t)$ is proportional to the magnetic flux across a GS source at time t . A particular value of τ is not important if it is much shorter than the burst.

If the flare process operated self-similarly throughout the burst, then the ratio of energy released in the current sheet during τ [$W(\tau, t) = \int_t^{t+\tau} q dt = q\tau = BZ\Psi(\tau, t)/2\pi$] to the total energy of electrons produced at the same time [$W^{\text{GS}}(\tau, t)$] was constant, *i.e.* $W^{\text{GS}}(\tau, t) \propto W(\tau, t)$. This relation is correct as long as the vertical size $[Z]$ of the current sheet is constant and the magnetic field $[B]$ in its vicinity is uniform. The latter assumption is justified by the rapid disappearance with increasing height of the small magnetic features associated with the strongly inhomogeneous photospheric magnetic field.

With a power-law energy distribution of GS-emitting electrons $[n(\epsilon)d\epsilon = K\epsilon^{-\delta}d\epsilon$ ($\epsilon_0 \leq \epsilon \leq \infty$)], their energy density is $\mathcal{E}_N = [(\delta - 1)/(\delta - 2)]\epsilon_0 N \equiv \bar{\epsilon}N$ [erg cm⁻³], $\delta > 2$. Here $n(\epsilon)$ is the number of electrons per cm³ in a unit interval of energy $[\epsilon]$, $N = \int n(\epsilon)d\epsilon$ is

the total number of GS-emitting electrons in 1 cm^3 , and $\bar{\epsilon}$ is the average energy of a single electron.

Since $W^{\text{GS}}(\tau, t) = N_{\text{tot}}(t)\bar{\epsilon}$, from the condition $W^{\text{GS}}(\tau, t) \propto W(\tau, t)$ we obtain the final equation for the total number of GS-emitting electrons: $N_{\text{tot}}(t) = \text{const} \times BZ\Psi(\tau, t)/\bar{\epsilon} \propto \Psi(\tau, t)$. Note that B is here related to the vicinity of the current sheet. In turn, $\Psi(\tau, t)$ is an instantaneous magnetic flux within one of the ribbon stripes: $\Psi(\tau, t) \equiv \Psi^{\text{stripe}}(t)$. The relation between the emission flux and the total number of emitting electrons [$F(t) \propto N_{\text{tot}}(t)$] is transformed into $F(t) \propto \Psi^{\text{stripe}}(t)$.

The similar evolution of the microwave sources observed by two radio heliographs and flare ribbons observed in UV and the similarity of microwave images and convolved UV images motivated us to use a model source system referring to the ribbons to simulate the GS emission in this event.

3.2. Modeling of Gyrosynchrotron Emission

The spectrum of the nonthermal microwave emission in the 26 December 2001 event has two conspicuous features: a persistent shape with weak changes in the peak frequency under large flux variations, and an enhanced low-frequency part. Melnikov, Gary, and Nita (2008) found the peak-frequency variations to be small in about one third of the events. The authors related this behavior to GS self-absorption around the peak of the burst and to the Tsytoich–Razin suppression in its early rise and late decay. Stähli, Gary, and Hurford (1989) did report the latter effect; however, its importance at the rise of a long-duration flare is difficult to reconcile with chromospheric evaporation. It is quantified by the Neupert effect (Neupert, 1968), *i.e.* by the similarity between the soft X-ray flux (directly dependent on the plasma density) and the antiderivative of the microwave burst. The plasma density is initially low, reducing the Tsytoich–Razin effect at this stage. At the decay of our burst, *viz.* at 05:29, the net total area at 34 GHz was $A \approx 2.3 \times 10^{19} \text{ cm}^2$ (Figure 5c), emission measure estimated from GOES data $\text{EM} \approx 4 \times 10^{49} \text{ cm}^{-3}$ (Article I), and plasma density $\approx (\text{EM}/A^{3/2})^{1/2} \approx 1.9 \times 10^{10} \text{ cm}^{-3}$. With the magnetic-field strength of $B \approx 540 \text{ G}$ estimated in Article I at 05:20, the Razin frequency was $\nu_{\text{R}} = 2\nu_{\text{p}}^2/(3\nu_{\text{B}}) \approx 0.68 \text{ GHz} \ll \nu_{\text{peak}} \approx 5.5 \text{ GHz}$ (Figure 10c). Thus, the ideas of Melnikov, Gary, and Nita (2008) are unlikely to help us because the magnetic fields of $\leq 300 \text{ G}$ that they considered are too weak for our sunspot-associated flare.

To account for the low-frequency increase in a GS spectrum, inhomogeneity of the source and superposition of multiple sources have been proposed (*e.g.* Alissandrakis and Preka-Papadema, 1984; Alissandrakis, 1986; Lee, Gary, and Zirin, 1994; Kuznetsov, Nita, and Fleishman, 2011). The main inhomogeneity in these models is related to the magnetic field in a flare loop with a varying cross section. This undoubted inhomogeneity affects the shape of the spectrum, especially its optically thick part (Bastian, Benz, and Gary, 1998; Kundu *et al.*, 2009). It is difficult to understand why the spectrum from a single inhomogeneous loop had a constant shape, while indications of multiple sources are certain.

We are not aware of inhomogeneous multi-loop models. To verify our interpretations, we are forced to use a tentative simplified modeling of GS emission from a set of several homogeneous sources. We are interested in general features of this system and need a very simple analytic description of GS emission, which the Dulk and Marsh (1982) approximations present. Their reduced accuracy at the lowest and highest harmonics of the gyrofrequency is not crucial for the task of the model, which is to understand the properties of our event.

Our model contains a considerable number of homogeneous GS sources, each with a different magnetic-field strength and volume. Their number depends on the width and length

of the brightest parts of the UV ribbons. The model should also demonstrate the direct dependence of the total flux and spectrum of the microwave emission on the total magnetic flux and its distribution over each of the ribbons. The model does not consider the influence of the ambient plasma on the generation and propagation of the GS emission, *i.e.* the Tsytovich–Razin effect and free–free absorption, which are very likely not important in our event.

The loop system constitutes an arcade rooted in the ribbons. Each ribbon in our event is extended and inhomogeneous in brightness and width. We relate a set of microwave sources to a brightest, broadest stripe of each ribbon. Its width $[\Delta^0]$ corresponds to a typical transverse size of a loop, whose end is rooted in this ribbon. The width of a loop varies according to the magnetic-field strength $[B]$ along it, being equal to $\Delta^0(B^0/B)^{1/2}$, with the superscript “0” related to the first ribbon. For a narrow ribbon stripe, the number of emitting loops $[m]$ should be about its length-to-width ratio. If the loops do not overlap, then their total flux $[F(t)]$ is the sum of the fluxes emitted by all of the loops.

Each i th loop is represented by two homogeneous cubic sources in its legs above both ribbons, corresponding to the observations at 5.7 and 17 GHz. Magnetic fluxes in conjugate cubes are equal to each other: $\Psi_i^E = \Psi_i^W$. The ratio of their sizes $[l_i^E/l_i^W]$ is determined by the ratio of the magnetic-field strengths in the east $[B_i^E]$ and the west source $[B_i^W]$, so that $\Psi_i^{(E,W)} = B_i^E l_i^{E2} = B_i^W l_i^{W2}$. It is convenient to use a set of m loops, each of which encloses an equal magnetic flux $\Psi_i = \Psi^{\text{stripe}}/m$. This assumption ensures the balance of magnetic fluxes in conjugate legs of any loop, regardless of its location, and facilitates partition into m cubic sources. Two partition methods apply.

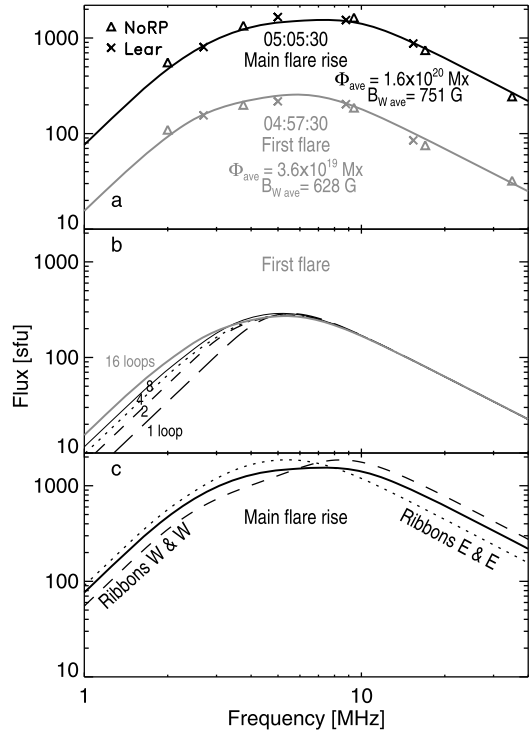
In the first method, the total magnetic flux Ψ^{stripe} is divided into m equal parts on the magnetogram within each ribbon in a fixed direction. The widths of the pieces can be different, while their magnetic fluxes are equal to each other. Each i th pair corresponds to a loop. The loops do not overlap, and the procedure to find B_i and l_i seems to be physically justified.

A rather formal second method considers the histograms $\{B, n(B)\}$ of the magnetic-field distribution within each ribbon, where $n(B)$ is the number of pixels where the magnetic-field strength is equal to B . The area below the histogram is divided into m equal parts corresponding to equal magnetic fluxes Ψ^{stripe}/m , which is easy to calculate. The cubic sources obtained in this way are different, and their paired link is lost. On the other hand, the scatter of the size and magnetic-field strength is maintained, as in the first partition method. We use the second method, which is simpler to implement.

The spectral flux density $F_i(\nu)$ from each i th unpolarized source is $F_i(\nu) = 2kT_{\text{eff}i}(\nu)[1 - \exp(-\tau_i(\nu))](\nu^2/c^2)A_i/R^2$, where k is the Boltzmann constant, A_i the source area, $R = 1$ AU, and $\tau_i(\nu) = \kappa_i(\nu)l_i$ the optical thickness. The effective temperature $[T_{\text{eff}i}(\nu)]$ and absorption coefficient $[\kappa_i(\nu)]$ are calculated following Dulk and Marsh (1982). In their Figure 3, the log–log plots of T_{eff} and κ deviate at low ν/ν_B from the quasi-linear parts into opposite directions, which reduces the errors (Kundu *et al.*, 2009). The deviations are smaller for $\delta < 3.5$ in our case. The total-flux spectrum is a sum of $2m$ spectra from all sources. The number density of microwave-emitting electrons $[N]$ and their power-law index $\delta = (2.7–3.0)$ are identical for all sources. The viewing angles of the sources in the legs of the loops above the east and west ribbons θ^E and θ^W are different, while their half-sum is the longitude of the flare site.

The optimal number of the paired sources $[m]$ was adjusted iteratively to meet three conditions: i) the sum of $2m$ sources provides a gradual spectrum with a single peak, ii) the value of m is about the ribbon length-to-width ratio, and iii) the model acceptably fits the observed spectrum. With an optimal number $[m]$, the field strengths $[B_i^{(E,W)}]$ estimated from

Figure 11 Results of the modeling. a) Observed (symbols) and modeled (lines) GS spectra in the first flare (gray) and at the main flare rise (black). b) The spectra in the first flare modeled with a different number of emitting loops from 1 to 16. c) The influence on the spectrum of asymmetry in the magnetic configuration: real configuration (solid), symmetric configuration with a magnetic-field distribution corresponding to the east ribbon at both sides (dotted), and the same with that of the west ribbon at both sides (dashed).



the photospheric magnetogram should be corrected to the coronal values. It is possible to use a constant scaling factor μ , so that the magnetic-field strengths in coronal sources are $\mu B_i^{(E,W)}$.

To estimate μ , we refer to Lee, Nita, and Gary (2009), who found an average magnetic field of $\bar{B} \approx 400$ G using a homogeneous GS source model and a scaling law between \bar{B} and the total area of a source. An intuitive option to calculate μ as a ratio of 400 G to an average field strength measured from the magnetogram within the ribbons leads to a biased estimate because the microwave flux depends in a nonlinear way on the magnetic field.

With any number of the sources, the flux at optically thin frequencies [$\tau(\nu) \ll 1$] is controlled by the total number of emitting electrons and their emissivity. Thus, $F_i(\nu) = \text{const.} \times N B_i^\alpha l_i^3 \nu^{1-\alpha} (\sin \theta)^{0.65\delta-0.43} 10^{0.52\delta}$ with $\alpha = 0.9\delta - 0.22$; θ is the viewing angle (Dulk and Marsh, 1982). The constancy of the optically thin total flux emitted by the same electron population with any number of the sources, up to a single large one (subscript ‘‘S’’), results in an equality $\sum N_i l_i^3 B_i^\alpha = N_S l_S^3 B_S^\alpha$. Using the constancy of the total number of emitting electrons [$\sum N_i l_i^3 = N_S l_S^3$] we obtain an average magnetic-field strength in an equivalent single source $B_S = \sum N_i l_i^3 B_i^\alpha / \sum N_i l_i^3$. Finally, we have estimated $\bar{B} = \mu B_S \approx 400$ G for the sources above each ribbon separately and obtained $\mu \approx 0.56$. In this approach, the magnetic flux [Ψ_i] is retained, and the change from B_i to μB_i results in a corresponding change in the size of each i th source from l_i to $l_i / \sqrt{\mu}$.

Figure 11a presents the results of the modeling by the gray line for the first flare (episode 1) and the black line for the rise of the main flare (episode 2). These two episodes occurred soon after fresh injections, when emission of trapped electrons, which we do not consider, can be neglected, and an assumption of a constant $\delta = 3.0$ is justified. The symbols denote the observed fluxes. An enhancement at 2 GHz was due to a contribution from

plasma emission. The average magnetic flux over the ribbon stripe [Φ_{ave}] used in the modeling is specified for each episode. The average field strength above the west ribbon stripe [B_{Wave}] additionally affects the microwave flux at optically thin frequencies. The number density of electrons with energies > 10 keV was $N = 1.7 \times 10^6 \text{ cm}^{-3}$ in both episodes. The total number of electrons was $N_{\text{tot}1} = 1.9 \times 10^{33}$ in episode 1 and $N_{\text{tot}2} = 1.9 \times 10^{34}$ in episode 2.

In Section 3.1 we obtained $F(t) \propto \Psi^{\text{stripe}}(t)$ assuming the magnetic field to be uniform at both sides of the neutral line, which is not realistic. Nevertheless, the model takes a real inhomogeneity of the photospheric magnetic field into account and matches the real spectrum acceptably well. The relation between the magnetic flux and microwaves can be generalized to a variable magnetic field, considering the intrinsic dependence of the microwave flux on the magnetic field strength, $F \propto N B^\alpha I_S^3 = N_{\text{tot}} B^\alpha \propto \Psi^{\text{stripe}} B^\alpha$.

The ratio of the optically thin microwave fluxes in the two episodes in Figure 11a is 8.9, while the ratio of the magnetic fluxes within the ribbon stripes is 4.4. With $\alpha = 0.9\delta - 0.22 = 2.48$, the expected microwave flux ratio is $4.4 \times (751/628)^{2.48} \approx 6.9$, which agrees with the model result of 8.9 within 30 %. This seems to be acceptable with our simplified approach.

Figure 11b demonstrates the influence on the spectrum of the number of loops for episode 1. The increase in the number of loops elevates the low-frequency branch of the spectrum. The effect is similar to that of the source inhomogeneity. The ratio of the 16-loop to the single-loop spectrum at 2 GHz is 5.1 in this case. The lowest-frequency slope [2.9] corresponds to the classical GS spectrum.

Figure 11c illustrates the role of asymmetry in the magnetic configuration with the same magnetic-flux reconnection rate. The solid line corresponds to the real situation in episode 2. The dashed line represents the spectrum for a hypothetical situation, when both microwave-emitting regions were located above identical ribbons corresponding to the actual west ribbon. The dotted line represents a similar experiment with two east ribbons.

The strongest asymmetry effect at optically thin frequencies is illustrated by two extremities. The high-frequency flux from a highly asymmetric configuration is determined by a single source, and the flux is doubled in a symmetric configuration (two identical sources). The asymmetry effect varies between a factor of one and two. The same occurs for the opposite asymmetry. Thus, with the same magnetic-flux reconnection rate, the high-frequency flux can vary within a factor of four.

The actual ratios of the optically thin fluxes in Figure 11c are 1.26 between the dashed and solid lines and 1.40 between the solid and dotted lines. The asymmetry in this event increased progressively. The west ribbon expanded into the sunspot umbra, the east ribbon developed into weaker-field regions. To balance the magnetic flux, an increasing high-frequency emission from the stronger-field west regions must be accompanied by an increasing area of the weaker-field east region that elevated the low-frequency part of the spectrum. The spectrum shape remained nearly constant, in spite of large changes in the microwave flux.

The relevance of a homogeneous source and simplified expressions by Dulk and Marsh (1982) were discussed by Lee, Nita, and Gary (2009). As they showed, the usage of a scaling law between the average magnetic field and total source area makes the homogeneous model sufficient to estimate statistical characteristics of microwave bursts such as the peak flux and frequency and spectral index. Each elementary loop in our model is replaced by two homogeneous sources of different size and magnetic field. A set of 32 homogeneous sources reflects the inhomogeneity of the ribbons. The scaling factor needed to shift from their magnetic fields to those in microwave sources is based on the results of Lee, Nita, and Gary (2009). Our model also acceptably reproduces the spectra around the peak and at lower frequencies.

Modeling the circular polarization of the GS emission is complicated by the near-the-limb location of the flare site. Since the west microwave source is visible through quasi-transversal magnetic fields that are associated with the arcade, polarization reversal is expected in a wide frequency range. Thus, the polarization of each elementary source is a result of the interplay between the optical thickness and polarization reversal issues, both of which depend on frequency. This makes the analysis of the polarization of the west source and the total emission too complex.

The polarized emission of the east source can only be extracted in NoRH 17 GHz and SSRT 5.7 GHz images. For the degree of polarization of each optically thin elementary source we used the corrected formula from Dulk (1985), otherwise, we assigned an opposite polarization of 15 %. The results for episode 1 are (all negative; first observed, second model): [25, 48] % at 5.7 GHz, [68, 54] % at 17 GHz; for episode 2: [35, 55] % at 5.7 GHz, [67, 55] % at 17 GHz. The model reproduces the actual degree of polarization within a factor of two with a correct sign.

The outcome of our simple modeling can be summarized as follows:

- i) The observed properties of the GS spectrum are consistent with the emission from a distributed multi-loop system, *i.e.* the flare arcade.
- ii) The asymmetry of the magnetic configuration is important. The magnetic-flux balance requires larger areas at the weaker-field side that elevated the low-frequency part of the spectrum, shifting the peak frequency to the left. Inhomogeneities of the individual sources could increase this effect.
- iii) To reproduce the observed spectrum with realistic magnetic fields, a large increase in magnetic flux is required in the main flare (the average field strength changed only insignificantly). This result is consistent with the temporal correlation between the magnetic-flux change rate and HXR emission found by Asai *et al.* (2004), Miklenic *et al.* (2007), Miklenic, Veronig, and Vršnak (2009), who measured the magnetic flux within expanding parts of the ribbons.
- iv) The replacement of a distributed multi-loop system by a single loop is generally not equivalent and can result in a different shape of the spectrum, peak frequency, and their behaviors during the burst. This leads to the next item.
- v) Modeling a microwave-emitting loop initiated by Alissandrakis and Preka-Papadema (1984) has been developed into a powerful tool (Tzatzakis, Nindos, and Alissandrakis, 2008; Kuznetsov, Nita, and Fleishman, 2011). The models use real data of magnetic fields and take its inhomogeneity, anisotropy, and spatial distribution of electrons into account. A next-step challenge is a realistic multi-loop model, at least for simplified conditions. Some elements of the scheme presented here might be helpful in its development.

3.3. Motions of Flare Sources

As known from observations in the H α line, flare kernels and ribbons initially approach each other along the neutral line, and then move away from it. The expansion of the ribbons was explained by the two-dimensional (2D) standard flare model. The motions along the neutral line have not been clearly visualized. Various motions observed later in HXR were summarized by Bogachev *et al.* (2005). The authors interpreted them in terms of the 2D model; their cartoons implied a questionable rotation of the current sheet around the vertical axis.

The motions along the neutral line have reasonably been considered as an intrinsically 3D effect. Its scheme was presented by Ji *et al.* (2008). The authors assumed a contraction of reconnected loops to be a necessary element of the unshearing process, whereas the two

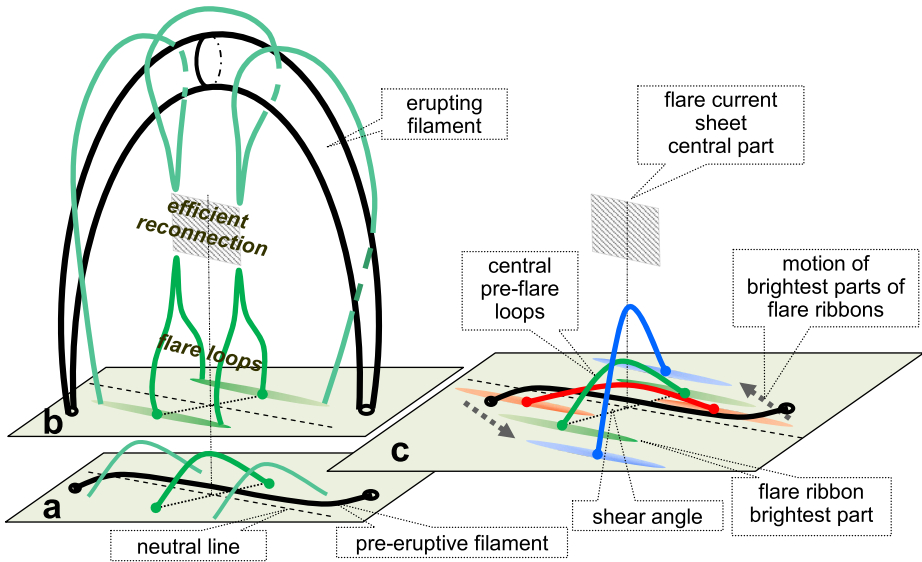


Figure 12 Decrease in shear between the brightest parts of the ribbons in terms of a 3D flare model. a) Before eruption. The base corresponds to the photosphere. The filament (thick black) is a flux-rope progenitor. Three coronal loops (green) belong to a single magnetic surface. b) Expansion of the filament and evolution of magnetic-field lines during eruption and flare. The brightest segments of the ribbons (green stripes) correspond to the most efficient central part of the current sheet. The centers of the stripes coincide with the footpoints of the middle loop in panel a. c) Combination of panels a and b. The red, green, and blue loops belong to different magnetic surfaces. The tops of these loops are located below the central part of the future current sheet. Their footpoints correspond to the brightest segments of the future ribbons (red, green, and blue stripes). The shear between the footpoints of the central loops decreases outward, from the red stripe to the green stripe, and then to the blue stripe.

phenomena seem to be different results of the flare reconnection that are not directly related with each other.

Reznikova *et al.* (2010) reported microwave observations of the motions along the neutral line. The authors noted that an M2.6 flare developed along the arcade that is visible in the $H\alpha$ and extreme-UV images and that at least several loops were involved in the process. However, they considered a single loop for each instance. In the discussion of the unshearing motions they mostly follow Ji *et al.* (2008).

The motions of the microwave sources in our event corresponded to those of the brightest parts of the ribbons, which we call the ribbon stripes for brevity. Figure 12 explains the relative displacement of the stripes. The intrinsic 3D geometry implies the presence in an extended current sheet of a zone of most efficient energy release, where the reconnection process is most similar to the 2D model. The formation of the main stripes is associated with this zone. Figures 12a and 12b present the evolution of three magnetic loops that reconnected in this zone. Initially, these loops belonged to a certain layer of magnetic arcades above the pre-eruptive filament. The dotted line connects the bases of the central loop to show the shear. Figure 12c shows the central loops of different layers. The higher a loop, the smaller the shear of its bases. The loops evolve similarly to the central loop in Figures 12a and 12b. The main stripes corresponding to these loops are displaced, as the arrows show, reflecting the decrease in shear with increasing height of the pre-eruptive arcade.

The main motions initially occurred nearly along the neutral line and away from it during the main flare phase and afterwards. This behavior (not shown in Figure 12) is associated

with a nonuniform decrease of the shear away from the neutral line. A similar behavior is exhibited by helical lines of a cylindrical nonlinear force-free magnetic field ($\nabla \times \mathbf{B} = \alpha \mathbf{B}$) when $\alpha \rightarrow 0$ with $r \rightarrow \infty$.

3.4. Configurations Responsible for Thermal and Nonthermal Emissions

Nonthermal emissions are generated by energetic electrons and carry the most direct information about acceleration processes in flares. As noted in Section 1, nonthermal sources observed in HXR and microwaves are usually simple and confined, which favors their identification with one or two flaring loops. This view drawn from microwave observations of almost all impulsive flares has been generalized to some major long-duration flares (Tzatzakis, Nindos, and Alissandrakis, 2008). Still stronger confinement is typical of HXR sources; complex structures like extended ribbons were observed in exceptional events (Masuda, Kosugi, and Hudson, 2001; Metcalf *et al.*, 2003; Liu *et al.*, 2007). In contrast, observations of flares in thermal emissions (H α line, UV, extreme UV, SXR) typically show complex multicomponent structures of a larger extent. This dissimilarity has led to different views on flaring structures drawn from different observations.

On the other hand, a synergy between the structures observed in thermal and nonthermal emissions has previously been conjectured, including studies in which some of us participated (Grechnev and Nakajima, 2002; Grechnev, Kundu, and Nindos, 2006; Kundu *et al.*, 2009). The causes of the differences between nonthermal sources and configurations visible in thermal emissions were unclear.

A key idea by Masuda, Kosugi, and Hudson (2001) to explain this difference has not been commonly recognized. The authors pointed out the limitations on the sensitivity and dynamic range (typically ≈ 10) in the HXR imaging. Indeed, images in HXR and γ -rays have been provided by the imagers of Fourier-synthesis type with an intrinsically limited coverage of the (u, v) -plane. These are the *Hard X-ray Telescope* (HXT: Kosugi *et al.*, 1991) onboard *Yohkoh* and the *Reuven Ramaty High-Energy Solar Spectroscopic Imager* (RHESSI: Lin *et al.*, 2002; Hurford *et al.*, 2002). Sources weaker than 10 % of the brightest one are not detectable in their images (Krucker *et al.*, 2014). Asai *et al.* (2002) also found that HXR sources accompanied the H α kernels only in the strongest magnetic fields: “The HXR sources indicate where large energy release has occurred, while the H α kernels show the precipitation sites of nonthermal electrons with higher spatial resolution”.

Flares have also been imaged in microwaves almost exclusively with Fourier-synthesis interferometers (mainly NoRH). They provide a better coverage of the (u, v) -plane than HXR imagers. On the other hand, optically thin GS emission strongly depends on the magnetic field $\propto B^\alpha$ with $\alpha = 2.5-4$. With the dynamic range of NoRH of ≈ 300 (Koshiishi *et al.*, 1994), its opportunities of observing weaker nonthermal structures seem to be comparable to HXR imagers. Moreover, microwave telescopes have a poorer spatial resolution than HXR imagers.

For these reasons, the strongest nonthermal sources are only expected in HXR and microwave images without weaker structures because of instrumental limitations. Configurations in which accelerated electrons are manifested, and those visible in thermal emissions, must be closely associated with each other.

Both thermal and nonthermal emissions in our event originated in basically the same configuration. Dissimilarities between the structures visible in microwaves and UV were mainly due to different spatial resolution and the dynamic range of the instruments and different dependencies of the emissions on the magnetic-field strength. Zimovets, Kuznetsov, and Struminsky (2013) also concluded that at least some of the single-loop configurations

in NoRH images corresponded to multi-loop arcades observed with telescopes of a higher spatial resolution.

An appropriate proxy for a configuration responsible for nonthermal emissions may be a structure observed in extreme ultraviolet or in soft X-rays. This expectation corresponds to widely accepted model concepts of eruptive flares (processes in confined flares are unlikely to be different in nature – see, *e.g.*, Thalmann *et al.*, 2015). This needs to be thoroughly verified. If this is correct, then considerations of simple configurations are justified when they appear as such in thermal emissions. Inevitable simplifications need to be recognized to avoid inadequate conclusions.

4. Summary and Concluding Remarks

We have studied the 26 December 2001 eruptive flare by combining the TRACE 1600 Å and NoRH 17 and 34 GHz images, the results obtained in [Article I](#) from the SSRT 5.7 GHz images, and different data. The analysis has shown that the first flare and the main flare were most likely associated with separate eruptions.

4.1. Milestones of the Event

The first eruption presumably occurred in AR 9742 around 04:40 and produced ejecta that did not appear in the LASCO field of view, but manifested itself in a slowly drifting radio burst. A related moderate two-ribbon flare involved medium magnetic fields, produced a moderate microwave burst up to a few hundred sfu at 5–6 GHz, and reached a GOES importance of M1.6. This flare lasted half an hour and had not fully decayed when another eruption occurred in AR 9742.

The second eruption occurred around 05:04 and produced a fast CME. The flare passed into the main two-ribbon flare and reached a strength of M7.1. The east ribbon observed in the first flare lengthened and broadened farther into regions of moderate and weak magnetic fields. The west ribbon entered the strongest magnetic fields above the sunspot umbra. The flare magnetic configuration was increasingly asymmetric. The microwave burst increased up to 4000 sfu at 6–7 GHz and 780 sfu at 35 GHz, and lasted about 15 minutes (FWHM).

Furthermore, TRACE images reveal a jet-like eruption around 05:09. Its light curve in 1600 Å is a spike with a FWHM duration as short as three minutes. The jet is not detectable in microwaves and will be analyzed in [Article III](#).

The first flare and the following main one were most likely caused by the first and second eruptions, respectively. The eruptions stretched closed magnetic configurations and thus could facilitate escape of particles accelerated in the active region. Sharp eruptions might have produced shock waves, which could also accelerate heavy particles. [Article III](#) will consider these possibilities.

4.2. Flare Morphology, Microwave Burst, and Proton Outcome

A conspicuous morphologic manifestation of a large-particle event is flaring above the sunspot umbra (Grechnev *et al.*, 2013b). This feature indicates involvement in flare processes of the strongest magnetic fluxes, whose reconnection rate corresponds to flare energy release and governs particle acceleration. The flare ribbons in the events analyzed previously overlapped with the umbras of opposite-polarity sunspots. The SOL2005-01-20 (GLE69) and SOL2006-12-13 (GLE70) events studied in detail exhibited large variations of the peak frequency, whose maximum exceeded 25 GHz, and peak fluxes at 35 GHz exceeded 10^4 sfu.

While the major flare in the SOL2001-12-26 event looks similar to these events, its morphological difference is the involvement in the flare of a single sunspot.

The microwave flux directly reflects the magnetic-flux reconnection rate, being proportional to its instantaneous value multiplied by a factor of $B^{0.98-0.22}$ at optically thin frequencies. The main difference between the moderate first flare and the much stronger main flare was in the reconnected magnetic flux, while parameters of the acceleration process manifesting in the number density and power-law index of accelerated electrons remained almost unchanged.

With the same magnetic-flux reconnection rate (and presumably the same production of accelerated particles), the microwave response strongly depends on the magnetic fields, including symmetry of the configuration. If it is asymmetric, then the microwave spectrum is broader, the peak frequency is lower, and its variations are small. The asymmetry of the configurations can cause an additional scatter within a factor of four in the correlations between high-frequency microwave bursts and near-Earth proton fluxes. An indication of asymmetry is overlap of the flare ribbon(s) with the umbra of a single, or two, or no sunspot.

The two flare parts were typical arcade flares, whose development is described by the 3D model. Its intrinsic phenomena are the motions of the arcade legs visible in microwaves with their bases visible as the ribbons. Their initial approach nearly along the neutral line reflects consecutive involvement in reconnection of structures corresponding to the pre-eruptive magnetic-field vector distribution. It is similar to that in a nonlinear force-free flux rope, *i.e.* from strongly sheared low structures to those less sheared located at increasing distances from the axis. A later expansion of the ribbons is accounted for by the 2D model.

In spite of an apparently single-loop configuration visible in microwave images, the correspondence between the positions and motions of the UV ribbons and nonthermal microwave sources shows that accelerated electrons emitted microwaves from the multi-loop arcade rooted in the UV ribbons. This conclusion is supported by a simple modeling of the microwave spectrum. Configurations with more than one loop appear to be common in various flares: from small, spiky events (Kundu, Nindos, and Grechnev, 2004) to large, long-duration events (Grechnev *et al.*, 2013a and the present article). Our analysis has demonstrated that dissimilarities between the structures visible in nonthermal and thermal emissions are due to different instrumental characteristics and different dependencies of the emissions on the magnetic field. In accordance with well-known models, a proxy of a configuration responsible for nonthermal emissions could be a structure observed in thermal emissions.

Acknowledgments We thank N.V. Nitta for discussions and the reviewer for useful remarks. We thank the instrument teams managing SSRT, NoRH, and NoRP; TRACE (NASA); SOHO/MDI and LASCO (ESA and NASA), GOES; USAF RSTN Network; NICT (Japan); and the CME Catalog at the CDAW Data Center (NASA and Catholic University of America). In memory of T.A. Treskov, one of the main developers of the SSRT, and N.N. Kardapolova, who managed SSRT observations for many years. This study was supported by the Russian State Contract No. IL.16.1.6. A. Kochanov was supported by the Russian Foundation of Basic Research under grants 15-32-20504 mol-a-ved and 15-02-03717. V. Kiselev was supported by the Marie Curie PIRSES-GA-2011-295272 RadioSun project.

Disclosure of Potential Conflicts of Interest The authors declare that they have no conflicts of interest.

References

- Alissandrakis, C.E.: 1986, *Solar Phys.* **104**, 207. DOI.
Alissandrakis, C.E., Preka-Papadema, P.: 1984, *Astron. Astrophys.* **139**, 507.

- Asai, A., Masuda, S., Yokoyama, T., Shimojo, M., Isobe, H., Kurokawa, H., Shibata, K.: 2002, *Astrophys. J. Lett.* **578**, L91. DOI.
- Asai, A., Yokoyama, T., Shimojo, M., Masuda, S., Kurokawa, H., Shibata, K.: 2004, *Astrophys. J.* **611**, 557. DOI.
- Aschwanden, M.J.: 2012, *Space Sci. Rev.* **173**, 3. DOI.
- Bastian, T.S., Benz, A.O., Gary, D.E.: 1998, *Annu. Rev. Astron. Astrophys.* **36**, 131. DOI.
- Bogachev, S.A., Somov, B.V., Kosugi, T., Sakao, T.: 2005, *Astrophys. J.* **630**, 561. DOI.
- Brueckner, G.E., Howard, R.A., Koomen, M.J., Korendyke, C.M., Michels, D.J., Moses, J.D., Socker, D.G., Dere, K.P., Lamy, P.L., Llebaria, A., *et al.*: 1995, *Solar Phys.* **162**, 357. DOI.
- Cheng, X., Zhang, J., Liu, Y., Ding, M.D.: 2011, *Astrophys. J. Lett.* **732**, L25. DOI.
- Cliver, E.W.: 2006, *Astrophys. J.* **639**, 1206. DOI.
- Dierckxsens, M., Tziotziou, K., Dalla, S., Patsou, I., Marsh, M.S., Crosby, N.B., Malandraki, O., Tsiropoula, G.: 2015, *Solar Phys.* **290**, 841. DOI.
- Dulk, G.A.: 1985, *Annu. Rev. Astron. Astrophys.* **23**, 169. DOI.
- Dulk, G.A., Marsh, K.A.: 1982, *Astrophys. J.* **259**, 350. DOI.
- Filippov, B., Golub, L., Koutchmy, S.: 2009, *Solar Phys.* **254**, 259. DOI.
- Gopalswamy, N., Xie, H., Yashiro, S., Akiyama, S., Mäkelä, P., Usoskin, I.G.: 2012, *Space Sci. Rev.* **171**, 23. DOI.
- Grechnev, V.V.: 2003, *Solar Phys.* **213**, 103. DOI.
- Grechnev, V.V.: 2004, In: Stepanov, A.V., Benevolenskaya, E.E., Kosovichev, A.G. (eds.) *Multi-Wavelength Investigations of Solar Activity*, *IAU Symp.* **223**, 625. DOI.
- Grechnev, V.V., Kochanov, A.A.: 2016, *Solar Phys.* 291. DOI (Article I).
- Grechnev, V.V., Nakajima, H.: 2002, *Astrophys. J.* **566**, 539. DOI.
- Grechnev, V.V., Kundu, M.R., Nindos, A.: 2006, *Publ. Astron. Soc. Japan* **58**, 47. DOI.
- Grechnev, V.V., Lesovoi, S.V., Smolkov, G.Y., Krissinel, B.B., Zandanov, V.G., Altyntsev, A.T., Kardapolova, N.N., Sergeev, R.Y., Uralov, A.M., Maksimov, V.P., Lubyshev, B.I.: 2003, *Solar Phys.* **216**, 239. DOI.
- Grechnev, V.V., Kurt, V.G., Chertok, I.M., Uralov, A.M., Nakajima, H., Altyntsev, A.T., Belov, A.V., Yushkov, B.Y., Kuznetsov, S.N., Kashapova, L.K., Meshalkina, N.S., Prestage, N.P.: 2008, *Solar Phys.* **252**, 149. DOI.
- Grechnev, V.V., Uralov, A.M., Chertok, I.M., Kuzmenko, I.V., Afanasyev, A.N., Meshalkina, N.S., Kalashnikov, S.S., Kubo, Y.: 2011, *Solar Phys.* **273**, 433. DOI.
- Grechnev, V.V., Kiselev, V.I., Uralov, A.M., Meshalkina, N.S., Kochanov, A.A.: 2013a, *Publ. Astron. Soc. Japan* **65**(SP1), S9. DOI.
- Grechnev, V.V., Meshalkina, N.S., Chertok, I.M., Kiselev, V.I.: 2013b, *Publ. Astron. Soc. Japan* **65**(SP1), S4. DOI.
- Grechnev, V.V., Uralov, A.M., Chertok, I.M., Slemzin, V.A., Filippov, B.P., Egorov Ya, I., Fainshtein, V.G., Afanasyev, A.N., Prestage, N., Temmer, M.: 2014, *Solar Phys.* **289**, 1279. DOI.
- Grechnev, V.V., Kiselev, V.I., Meshalkina, N.S., Chertok, I.M.: 2015a, *Solar Phys.* **290**, 2827. DOI.
- Grechnev, V.V., Uralov, A.M., Kuzmenko, I.V., Kochanov, A.A., Chertok, I.M., Kalashnikov, S.S.: 2015b, *Solar Phys.* **290**, 129. DOI.
- Grechnev, V.V., Uralov, A.M., Kochanov, A.A., Kuzmenko, I.V., Prosovetsky, D.V., Egorov, Y.I., Fainshtein, V.G., Kashapova, L.K.: 2016, *Solar Phys.* **291**, 1173. DOI.
- Grechnev, V.V., Kiselev, V.I., Uralov, A.M., Klein, K.-L., Kochanov, A.A.: 2017, in preparation. *Solar Phys.* (Article III).
- Hanaoka, Y.: 1996, *Solar Phys.* **165**, 275. DOI.
- Hanaoka, Y.: 1997, *Solar Phys.* **173**, 319. DOI.
- Handy, B.N., Acton, L.W., Kankelborg, C.C., Wolfson, C.J., Akin, D.J., Bruner, M.E., Carvalho, R., Catura, R.C., Chevalier, R., Duncan, D.W., *et al.*: 1999, *Solar Phys.* **187**, 229. DOI.
- Hurford, G.J., Schmahl, E.J., Schwartz, R.A., Conway, A.J., Aschwanden, M.J., Csillaghy, A., Dennis, B.R., Johns-Krull, C., Krucker, S., Lin, R.P., *et al.*: 2002, *Solar Phys.* **210**, 61. DOI.
- Ji, H., Wang, H., Liu, C., Dennis, B.R.: 2008, *Astrophys. J.* **680**, 734. DOI.
- Kahler, S.W.: 1982, *J. Geophys. Res.* **87**, 3439. DOI.
- Kallenrode, M.-B.: 2003, *J. Phys. G, Nucl. Part. Phys.* **29**, 965. DOI.
- Koshiishi, H., Enome, S., Nakajima, H., Shibasaki, K., Nishio, M., Takano, T., Hanaoka, Y., Torii, C., Sekiguchi, H., Kawashima, S., *et al.*: 1994, *Publ. Astron. Soc. Japan* **46**, L33.
- Kosugi, T., Dennis, B.R., Kai, K.: 1988, *Astrophys. J.* **324**, 1118. DOI.
- Kosugi, T., Makishima, K., Murakami, T., Sakao, T., Dotani, T., Inada, M., Kai, K., Masuda, S., Nakajima, H., Ogawara, Y., Sawa, M., Shibasaki, K.: 1991, *Solar Phys.* **136**, 17. DOI.
- Krucker, S., Christe, S., Glesener, L., Ishikawa, S.-n., Ramsey, B., Takahashi, T., Watanabe, S., Saito, S., Gubarev, M., Kilaru, K., *et al.*: 2014, *Astrophys. J. Lett.* **793**, L32. DOI.
- Kundu, M.R., Nindos, A., Grechnev, V.V.: 2004, *Astron. Astrophys.* **420**, 351. DOI.

- Kundu, M.R., Grechnev, V.V., White, S.M., Schmahl, E.J., Meshalkina, N.S., Kashapova, L.K.: 2009, *Solar Phys.* **260**, 135. DOI.
- Kuznetsov, A.A., Nita, G.M., Fleishman, G.D.: 2011, *Astrophys. J.* **742**, 87. DOI.
- Lee, J.W., Gary, D.E., Zirin, H.: 1994, *Solar Phys.* **152**, 409. DOI.
- Lee, J., Nita, G.M., Gary, D.E.: 2009, *Astrophys. J.* **696**, 274. DOI.
- Lin, R.P., Dennis, B.R., Hurford, G.J., Smith, D.M., Zehnder, A., Harvey, P.R., Curtis, D.W., Pankow, D., Turin, P., Bester, M., et al.: 2002, *Solar Phys.* **210**, 3. DOI.
- Liu, C., Lee, J., Gary, D.E., Wang, H.: 2007, *Astrophys. J. Lett.* **658**, L127. DOI.
- Masson, S., Pariat, E., Aulanier, G., Schrijver, C.J.: 2009, *Astrophys. J.* **700**, 559. DOI.
- Masuda, S., Kosugi, T., Hudson, H.S.: 2001, *Solar Phys.* **204**, 55. DOI.
- Melnikov, V.F., Magun, A.: 1998, *Solar Phys.* **178**, 153. DOI.
- Melnikov, V.F., Gary, D.E., Nita, G.M.: 2008, *Solar Phys.* **253**, 43. DOI.
- Meshalkina, N.S., Uralov, A.M., Grechnev, V.V., Altyntsev, A.T., Kashapova, L.K.: 2009, *Publ. Astron. Soc. Japan* **61**, 791. DOI.
- Metcalf, T.R., Alexander, D., Hudson, H.S., Longcope, D.W.: 2003, *Astrophys. J.* **595**, 483. DOI.
- Miklenic, C.H., Veronig, A.M., Vršnak, B.: 2009, *Astron. Astrophys.* **499**, 893. DOI.
- Miklenic, C.H., Veronig, A.M., Vršnak, B., Hanslmeier, A.: 2007, *Astron. Astrophys.* **461**, 697. DOI.
- Nakajima, H., Sekiguchi, H., Sawa, M., Kai, K., Kawashima, S.: 1985, *Publ. Astron. Soc. Japan* **37**, 163.
- Nakajima, H., Nishio, M., Enome, S., Shibasaki, K., Takano, T., Hanaoka, Y., Torii, C., Sekiguchi, H., Bushimata, T., Kawashima, S., et al.: 1994, *Proc. IEEE* **82**, 705. DOI.
- Neupert, W.M.: 1968, *Astrophys. J. Lett.* **153**, L59. DOI.
- Nishio, M., Yaji, K., Kosugi, T., Nakajima, H., Sakurai, T.: 1997, *Astrophys. J.* **489**, 976. DOI.
- Nitta, N.V., Liu, Y., DeRosa, M.L., Nightingale, R.W.: 2012, *Space Sci. Rev.* **171**, 61. DOI.
- Reznikova, V.E., Melnikov, V.F., Ji, H., Shibasaki, K.: 2010, *Astrophys. J.* **724**, 171. DOI.
- Scherrer, P.H., Bogart, R.S., Bush, R.I., Hoeksema, J.T., Kosovichev, A.G., Schou, J., Rosenberg, W., Springer, L., Tarbell, T.D., Title, A., et al.: 1995, *Solar Phys.* **162**, 129. DOI.
- Smolkov, G.I., Pistolkors, A.A., Treskov, T.A., Krissinel, B.B., Putilov, V.A.: 1986, *Astrophys. Space Sci.* **119**, 1. DOI.
- Stähli, M., Gary, D.E., Hurford, G.J.: 1989, *Solar Phys.* **120**, 351. DOI.
- Thalmann, J.K., Su, Y., Temmer, M., Veronig, A.M.: 2015, *Astrophys. J. Lett.* **801**, L23. DOI.
- Torii, C., Tsukiji, Y., Kobayashi, S., Yoshimi, N., Tanaka, H., Enome, S.: 1979, *Proc. Res. Inst. Atmos.* **26**, 129.
- Trottet, G., Samwel, S., Klein, K.-L., Dudok de Wit, T., Miteva, R.: 2015, *Solar Phys.* **290**, 819. DOI.
- Tzatzakis, V., Nindos, A., Alissandrakis, C.E.: 2008, *Solar Phys.* **253**, 79. DOI.
- Uralov, A.M., Grechnev, V.V., Rudenko, G.V., Myshyakov, I.I., Chertok, I.M., Filippov, B.P., Slemzin, V.A.: 2014, *Solar Phys.* **289**, 3747. DOI.
- Vilmer, N., MacKinnon, A.L., Hurford, G.J.: 2011, *Space Sci. Rev.* **159**, 167. DOI.
- White, S.M., Krucker, S., Shibasaki, K., Yokoyama, T., Shimojo, M., Kundu, M.R.: 2003, *Astrophys. J. Lett.* **595**, L111. DOI.
- Yashiro, S., Gopalswamy, N., Michalek, G., St. Cyr, O.C., Plunkett, S.P., Rich, N.B., Howard, R.A.: 2004, *J. Geophys. Res.* **109**, A07105. DOI.
- Zimovets, I.V., Kuznetsov, S.A., Struminsky, A.B.: 2013, *Astron. Lett.* **39**, 267. DOI.
- Zimovets, I., Vilmer, N., Chian, A.C.-L., Sharykin, I., Struminsky, A.: 2012, *Astron. Astrophys.* **547**, A6. DOI.